Chapter 4

Circumnuclear Keplerian Disks in Galaxies[1]

Abstract

In this Chapter we demonstrate the possibility of inferring the presence of Keplerian gaseous disks using optical ground-based telescopes properly equipped. We have modeled the peculiar bidimensional shape of the emission lines in a sample of five S0-Sa galaxies as due to the motion of a gaseous disk rotating in the combined potential of a central point-like mass and of an extended stellar disk. The value of the central mass concentration estimated for four galaxies of the sample (NGC 2179, NGC 4343, NGC 4435 and NGC 4459) is $\sim 10^9$ M$_\odot$. For the remaining galaxy NGC 5064 an upper limit of 5×10^7 M$_\odot$ is estimated.

4.1 Introduction

There is an increasing evidence of conspicuous mass concentrations in the center of galaxies, lending support to the idea that their central engine is constituted by a black hole (see Kormendy & Richstone (1995), Ho (1998) for recent reviews). This evidence comes both from stellar and gaseous dynamics. In this latter case the mass concentration is deduced by the observation of an increase towards the center of the rotation velocity of the gaseous disk, according to the Kepler's third law. Seven circumnuclear Keplerian disks (hereafter CNKD) have been up to now observed: four have been discovered in elliptical galaxies using the high resolution capability of the *Hubble Space Telescope (HST)* (Ferrarese et al., 1996; Macchetto et al., 1997; Bower et al., 1998; van der Marel & van den Bosch, 1998), while three were detected in spirals with Very Long Baseline Interferometry (VLBI) and Very Long Baseline Array (VLBA) observations of maser sources (Miyoshi et al., 1995; Greenhill & Gwinn, 1997; Greenhill, Moran & Herrnstein, 1997).

In a program aimed to study with high spatial and spectral resolution the structure of the emission lines in the nuclear regions of early-type disk galaxies, we have obtained with the 3.6-m telescope at La Silla major axis spectra of the Sa galaxies NGC 2179 and NGC 5064. In the first case it is possible to recognize, applying our modeling technique, the

[1]Bertola, F., Cappellari, M., Funes, J. G., Corsini, E. M., Pizzella, A., & Vega Beltrán, J. C. 1998, ApJ, 509, L93, expanded version

Table 4.1: Parameters of the modeled galaxies.

object name (1)	type [RSA] (2)	type [RC3] (3)	B_T^0 [mag] (4)	P.A. [°] (5)	i [°] (6)	$V_\odot$ [km s^{-1}] (7)	D [Mpc] (8)	scale [pc$''^{-1}$] (9)	$M_{B,\rm bulge}$ [mag] (10)	$M_\bullet$ [10^8M$_\odot$] (11)
NGC 2179[a]	Sa	SAS0	12.83	170	51	2885±15	35.6	172.6	-19.07	10
NGC 5064[a]	Sa	PSA2*	11.67	38	65	2980±15	36.7	177.9	-19.78	< 0.5
NGC 4343[b]	···	SAT3*	12.37	133	78	1002±10	17.0	82.4	-17.24	5
NGC 4435[b]	$SB0_1(7)$	LBS0	11.61	13	90	806±10	17.0	82.4	-18.93	10
NGC 4459[b]	$S0_3(3)$	LAR+	11.21	110	42	1183±10	17.0	82.4	-19.20	10

[a] From our sample
[b] from the sample of Rubin et al. (1997)

Notes—Col. (2): morphological classification from Sandage & Tamman (1981). Col. (3): morphological classification from de Vaucouleurs et al. (1991, hereafter RC3). Col. (4): total B magnitude after correcting for extinction and redshift from RC3. Col. (5): major-axis position angle from RC3. Col. (6): inclination from Rubin et al. (1997) except for NGC 2179 and NGC 5064 (Tully 1988). Col. (7): heliocentric systemic velocity derived as the center of symmetry of the gas rotation curve. For NGC 2179, NGC 5064 it is taken from our data, and for NGC 4343, NGC 4435, NGC 4459 it is taken from Rubin et al. (1997). Col. (8): distance of NGC 2179 and NGC 5064 is derived from the heliocentric velocity corrected for the motion of the Sun with respect of the Local Group by $\Delta V = 300 \cos b \sin l$ with $H_0 = 75$ km s^{-1} Mpc^{-1}. The galaxies of the Rubin's sample are members of the Virgo cluster and we assumed a distance of 17 Mpc (Freedman et al. 1994). Col. (10): statistical estimate of the absolute B magnitude of the bulge derived following Simien & de Vaucouleurs (1986). Col. (11): value of the central mass concentration derived as described in Sect. 4.3.

kinematical behavior typical of a CNKD while the second represents a limiting case for its detection with our instrumental setup. In addition we apply our modeling to three early-type disk galaxies (NGC 4343, NGC 4435 and NGC 4459) observed by Rubin, Kenney & Young (1997), showing that also in these cases the shape of the emission lines is consistent with the presence of CNKDs. In this way we demonstrate the feasibility of detecting CNKDs with optical ground-based telescopes. The general data on the galaxies studied are given in Table 4.1.

4.2 Observations and data reduction

The spectroscopic observations of NGC 2179 and NGC 5064 were carried out at the 3.6-m ESO Telescope in La Silla on February 3-4, 1997. The telescope was equipped with the Cassegrain Echelle Spectrograph mounting the Long Camera in long-slit configuration without the crossdisperser. The 31.6 lines mm^{-1} grating was used in combination with a $1''\!.3\times2'\!.4$ slit. The spectral order #86 ($\lambda_c = 6617$ Å) corresponding to the redshifted Hα region was isolated by means of the narrow-band 6630/51 Å filter. It yielded a wavelength coverage of about 78 Å between 6593 Å and 6670 Å with a reciprocal dispersion of 3.17 Å mm^{-1}. The adopted detector was the No. 37 1024×1024 TK1024AB CCD with a 24×24 μm^2 pixel size. No on-chip binning was applied and each pixel corresponds to 0.076 Å×$0''\!.33$.

We took for NGC 2179 and NGC 5064 six and four separate major-axis spectra (P.A. = 170° and P.A. = 38° respectively) centered on the nucleus for a total exposure time of 360 and 240 minutes respectively. The galaxies were centered on the slit using the guiding camera at the beginning of each exposure. Comparison thorium-argon lamp exposures were obtained before and after each object integration. The value of the seeing FWHM during the observing nights was between $0''\!.8$ and $1''\!.2$ as measured by the La Silla Differential Image Motion Monitor. Using standard MIDAS routines the spectra were bias subtracted, flat-field corrected, cleaned for cosmic rays and wavelength calibrated. Cosmic rays were identified by comparing the counts in each pixel with the local mean and standard deviation, and then corrected by substituting a suitable value. The instrumental resolution was derived by measuring the FWHM of ~ 30 single emission lines distributed all over the spectral range of a calibrated comparison spectrum. It corresponds to a FWHM $= 0.233 \pm 0.017$ Å (i.e. ~ 11 km s^{-1} at Hα). The single spectra of the same object were aligned and coadded using their stellar-continuum centers as reference. In each spectrum the center of the galaxy was defined by the center of a Gaussian fit to the radial profile of the stellar continuum. The contribution of the sky was determined from the edges of the resulting frame and then subtracted. To study the Hα emission line, we subtracted the underlying stellar continuum which was determined by averaging a 2.5 Å wide region with high S/N adjacent to the Hα line. A constant stellar continuum provides a good match to the underlying distribution within this narrow wavelength range. For the purpose of this Chapter the subtraction of a continuum with the proper Hα absorption is not crucial since the same bidimensional shape is observed also in the [N II] λ6583 line. We did not model this line bacause it falls at the edge of the sensitivity curve.

In addition to the spectroscopic material narrow-band Hα imaging of NGC 2179 was performed on March 9-11, 1997 at the 1.8-m Vatican Advanced Technology Telescope. A back illuminated 2048$\times$2048 Loral CCD with 15×15 μm^2 pixels was used as detector at the aplanatic Gregorian focus, f/9. It yielded a field of view of $6\rlap{.}'4 \times 6\rlap{.}'4$ with an image scale of $0\rlap{.}''4$ pixel^{-1} after a 2×2 on-line pixel binning. We obtained 3×10 minutes emission-band images and 3×2 minutes Cousins $R-$band images. The emission-band images were taken with an interference filter ($\lambda_c = 6630$ Å; $\Delta\lambda_{\rm FWHM} = 70$ Å) isolating the spectral region characterized by the redshifted Hα and [N II] $\lambda\lambda$6548, 6583 emission lines. The data reduction was routine. Gaussian fit to field stars in the two final processed images yielded point spread function FWHM of $1\rlap{.}''0$. The continuum-free image of NGC 2179 showing the galaxy Hα+[N II] emission was obtained by subtracting the R-band image, suitably scaled, from the emission-band image.

4.3 Results

The complex bidimensional structure (in the velocity-position map) of the Hα emission line in NGC 2179 is shown in Fig. 4.1a. In the central region ($r \lesssim 2''$) the line is highly tilted and extends up to ± 250 km s^{-1}. The intensity distribution along the line shows two symmetric peaks and a central minimum at $r = 0$, $v = 0$. The shape of the emission is such that at $r = \pm 3''$ we observe $\Delta v = 200$ km s^{-1}. Proceeding further away from the center, Δv increases up to an almost constant value of 400 km s^{-1}.

In the following we demonstrate that the peculiar shape and intensity distribution of these emission lines is not produced by two kinematically distinct components as the appearance could suggest, but they are due to a unique velocity field traced by a thin gaseous disk rotating in the combined potential of a central point-like mass ($v \rightarrow \infty$ as $r \rightarrow 0$) embedded in an extended stellar disk and to the deterioration caused by the instrumental resolution and seeing. The presence of a gaseous disk in the principal plane of NGC 2179 is supported by our Hα image, which shows a smooth central structure characterized by the same ellipticity ($\epsilon \simeq 0.2$) and major-axis position angle (P.A. $\simeq 170°$) as those of the stellar content observed in the $R-$band. The bright knots present in the observed spectrum are due to spiral arms which are also visible in our Hα image.

We assume that the gas resides in an infinitesimally thin disk whose mean motion is

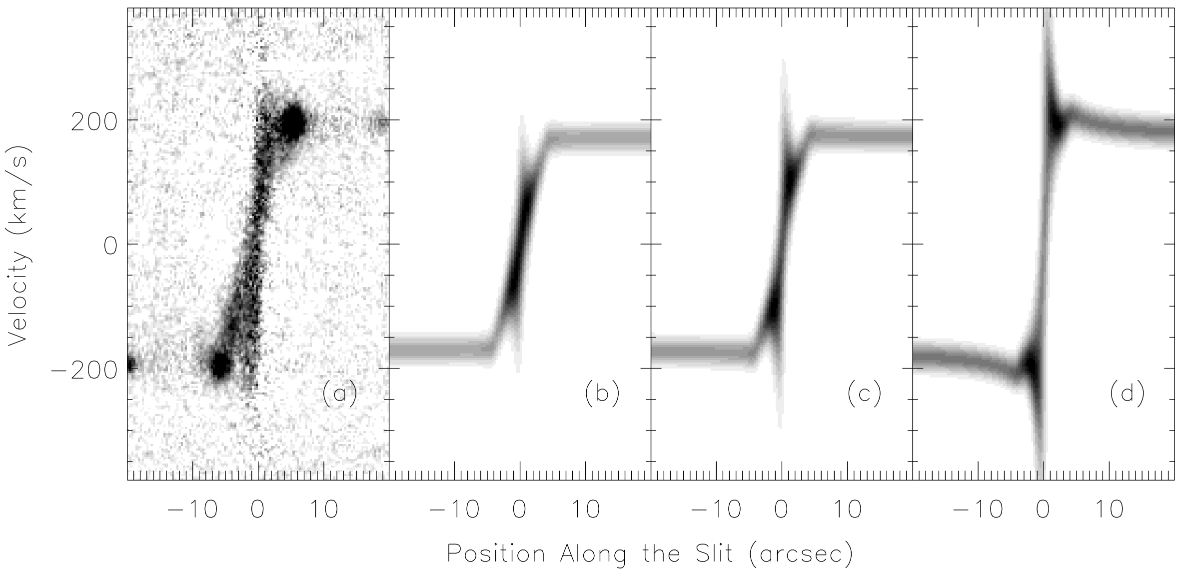

Figure 4.1: *(a):* The Hα emission line, observed along the major axis of NGC 2179, after subtraction of the stellar continuum. *(b), (c) and (d):* Models of the NGC 2179 Hα line [shown in the same scale of *panel (a)*] obtained with different point-like central masses. *(b):* $M_\bullet = 2\times10^8$ M$_\odot$. *(c):* $M_\bullet = 1\times10^9$ M$_\odot$ corresponding to our best-fit model. *(d):* $M_\bullet = 5\times10^9$ M$_\odot$.

characterized by circular orbits in the plane of the galaxy. At each position (x, y) on the sky the line-of-sight velocity profile is a Gaussian ϕ with mean $V(x, y) = V_c(R)\ x \sin i/R$ and dispersion $\sigma(R)$, where $R^2 = x^2 + (y/\cos i)^2$ is the radius in the disk and i (Table 4.1) the inclination of the galaxy. The dispersion is given by $\sigma^2(R) = \sigma^2_{gas}(R) + \sigma^2_{instr}$, where $\sigma_{gas}(R)$ is the intrinsic velocity dispersion of the gas and σ_{instr} is the instrumental dispersion (assuming a Gaussian instrumental broadening function). The gas dispersion is assumed to be isotropic and has been parametrized through $\sigma_{gas}(R) = \sigma_0 + \sigma_1 \exp(-R/R_t)$, where R_t is the scale length of the turbulence.

The circular velocity $V_c(R)$ is produced by the combined potential of a point-like mass $M_\bullet$ and of the disk-like stellar component. The contribution to the velocity due to the point-like mass is given by $V_\bullet(R) = \sqrt{GM_\bullet/R}$. The contribution $V_\star(R)$ due to the stars potential has been directly measured on the emission lines of each spectrum at distances where both the seeing effect and the point-like mass attraction are negligible, and it has been linearly interpolated for smaller R by imposing that $V_\star(0) = 0$. The linearity of this interpolation is not crucial for the model since in the inner regions the potential is dominated by the contribution of the central point-like mass concentration. The resulting intrinsic velocity profile of the disk is then computed as $V_c^2(R) = V_\bullet^2(R) + V_\star^2(R)$.

The bidimensional model of the emission lines is given by

$$\Phi(v, S) = \int_{S-\frac{\Delta s}{2}}^{S+\frac{\Delta s}{2}} \mathrm{d}s \int_{B-\frac{h}{2}}^{B+\frac{h}{2}} \mathrm{d}b \iint_{-\infty}^{+\infty} \mathrm{d}s'\,\mathrm{d}b'\,\phi[v - V(s', b')]\, I(s', b')\, P(s'-s, b'-b)$$

where (S, B) are the coordinate along the slit and perpendicularly to it respectively, while h is the slit width and Δs is the pixel size of the detector. $I(s', b')$ is the intrinsic surface brightness distribution of the disk and has been parametrized as $I(R) = I_0 + I_1 \exp(-R/R_I)$, where I_0, I_1 and R_I are free parameters. $P(s' - s, b' - b)$ is the PSF which has been modeled as a Gaussian, owing to the lack of a specific PSF image obtained at the time of the observations. Note that the parameterizations for $I(R)$ and $\sigma_{gas}(R)$ have been chosen because they are able to adequately reproduce our data, but they have no further physical significance. The line profile $\Phi(v, S)$, rebinned on a grid with steps Δv (reciprocal dispersion) and Δs, can be directly compared to the star-light-subtracted bidimensional spectrum obtained on the CCD.

In figure 4.2 we show an example of the above procedure, applied to the simulation of an observation with HST of the thin gaseous disk at the center of the elliptical galaxy M87. Using the same model, the velocity field shown in Figure 4.3 and the distance given in Table 4.1 we have obtained for NGC 2179 the simulation of the Hα emission line shown in Fig. 4.1c, which is remarkable for its similarity with the observed one (Fig. 4.1a). The bright knots in the spectrum due to the spiral arms have not been reproduced in our model. The point-like mass of the best-fit model is 1×10^9 M$_\odot$. It should be clear that our model shows only the consistency of the observations with the presence of a central point-like mass (black hole). However a central stellar density cusp could also fit the data. In order to estimate the errors in the central mass determination we have modeled the shape of the line for different central point-like masses. In Fig. 4.1b and Fig. 4.1d we show two extreme cases where the central mass is smaller and larger respectively by a factor 5 than the mass of the best fit. On the basis of visual comparison with the observations of a series of models we estimate that our error could not be larger than a factor 3 ($\log M_\bullet = 9.0 \pm 0.5$ in solar units).

The bidimensional shape of the Hα emission line in the second galaxy we observed, NGC 5064, is shown in Fig. 4.4a. Contrary to NGC 2179, it does not present any peculiar central structure. The line gives rise to a standard rotation curve with the inner rigid-body rotation extended up to $r = \pm 4''$, and followed by a flat portion ($\Delta v = 400$ km s^{-1}). By applying the same modeling technique as we did for NGC 2179 we computed the shape of the emission lines as a function of decreasing central mass until the complex structure described above tend to disappear. The limiting case corresponds to a central point-like mass of 5×10^7 M$_\odot$ and is illustrated in Fig. 4.4b. Comparing this model with the observed Hα line in NGC 5064 we deduce that in this galaxy either the central mass is lower than 5×10^7 M$_\odot$ or the unresolved Keplerian part of the gaseous disk does not give a detectable contribution.

Emission lines with a bidimensional shape and an intensity distribution similar to those observed in NGC 2179 have been observed also by Rubin et al. (1997). We have selected in their sample the most representative ones, namely NGC 4343 (Sa), NGC 4435 (S0) and NGC 4459 (S0). We applied our modeling techniques to reproduce their isophotal maps, taking into account their instrumental setup and seeing condition. The comparison between the observations and our models is shown in Fig. 4.5, and it appears quite satisfactory. In all the three cases the central tilted part of the emission is characterized by the absence of a central intensity peak, both in the model and in the observed line. The absence of the flat region of the rotation curve produced by the potential of the stellar disk in the case of NGC 4435 can be easily modeled by adopting $I_0 \simeq 0$. The values of the central masses are of the same order as that of NGC 2179 and are given in Table 4.1. A comparison between a set of model lines obtained with different central masses and the observations has been carried out for these galaxies, in the same way as we did for NGC 2179. We estimate that the masses given in Table 4.1 for the Rubin et al. (1997) galaxies are affected by uncertainties of the same order of magnitude as in NGC 2179.

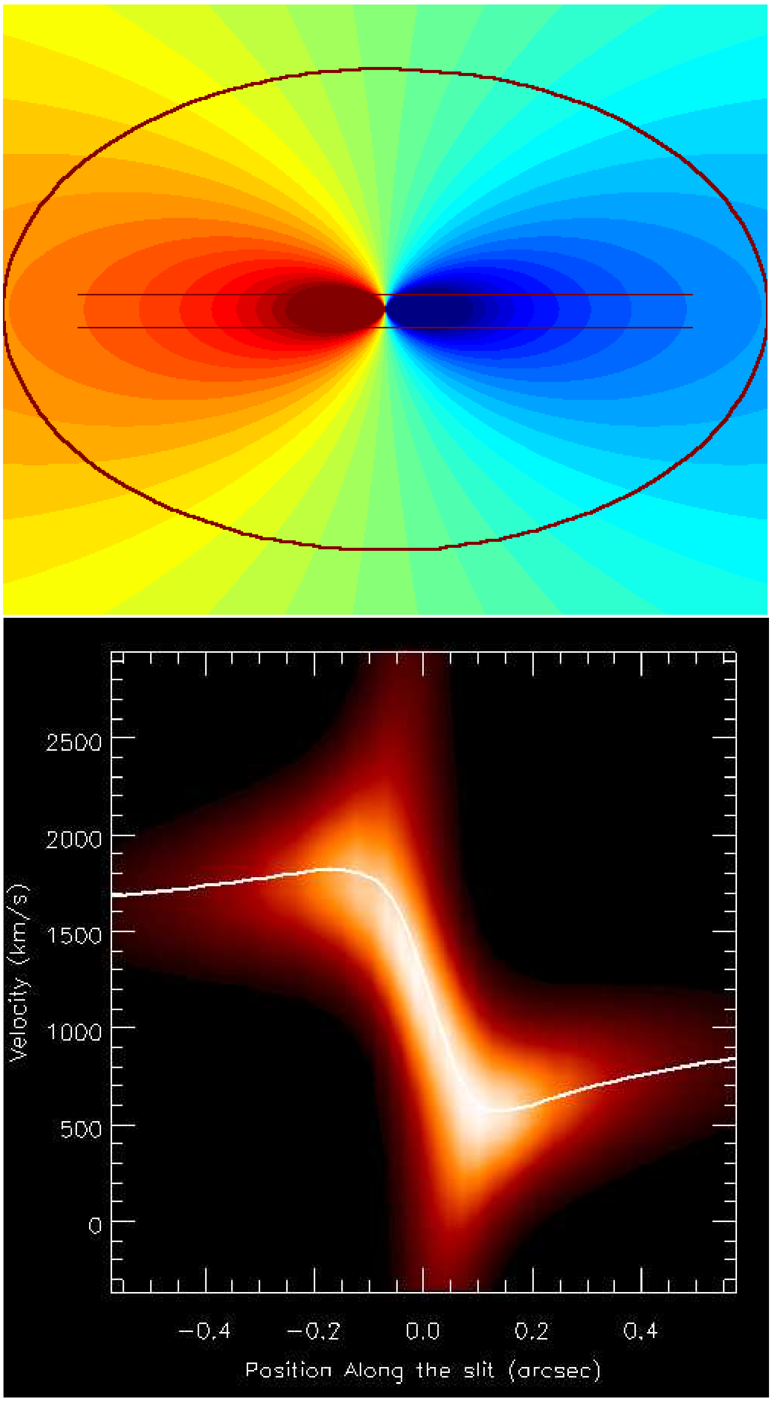

Figure 4.2: *Upper Panel:* Keplerian velocity field produced by a 3×10^9 $M_\odot$ Black Hole on a thin gaseous disk observed with an inclination of $\sim 50°$ at the distance of Virgo (17 Mpc). Superimposed is a $0\farcs06$ wide slit. The parameters mimic those for the BH in M87. *Lower Panel:* Simulation of a spectroscopic observation of the above gas disk with the HST/STIS. The solid line shows the velocity curve obtained by fitting a Gaussian to the columns of this spectrum.

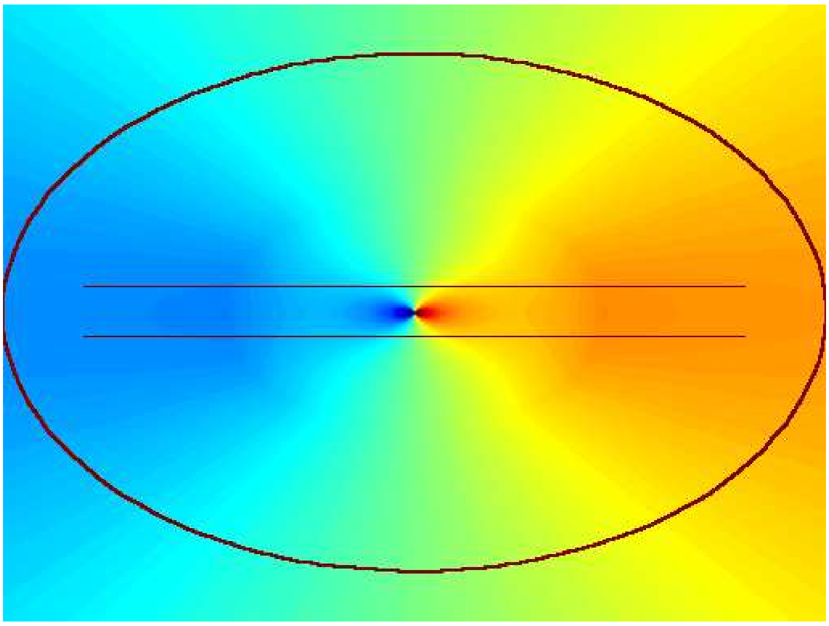

Figure 4.3: Model for the velocity field of an extended thin gaseous disk, in a spiral galaxy with central BH, at the distance of Virgo. In this example the velocity field is dominated by a 10^9 $M_\odot$ BH within $\approx 1''$ from the center, in the range $\approx 1'' - 5''$ the field has nearly rigid rotation, while the velocity becomes constant at larger radii. Superimposed is a $1''$ wide slit.

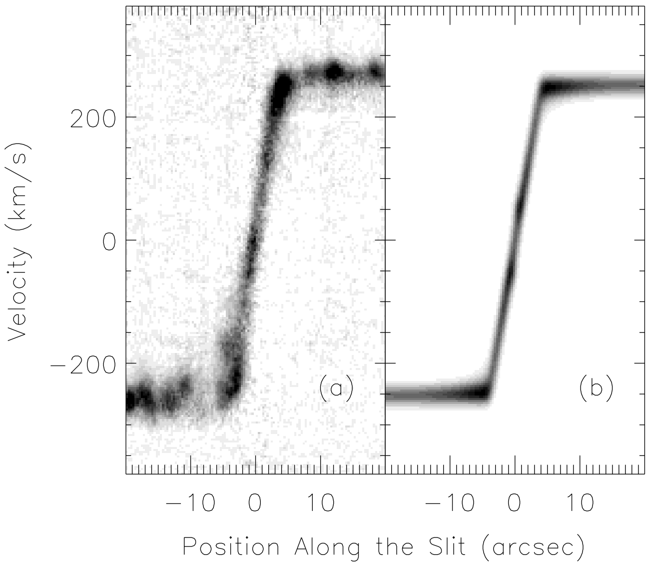

Figure 4.4: *(a):* The Hα emission line, observed along the major axis of NGC 5064, after subtraction of the stellar continuum. *(b):* Model of the NGC 5064 Hα line obtained with the highest point-like central mass which can be added without significantly disturbing the general shape of the line ($M_\bullet = 5 \times 10^7$ $M_\odot$).

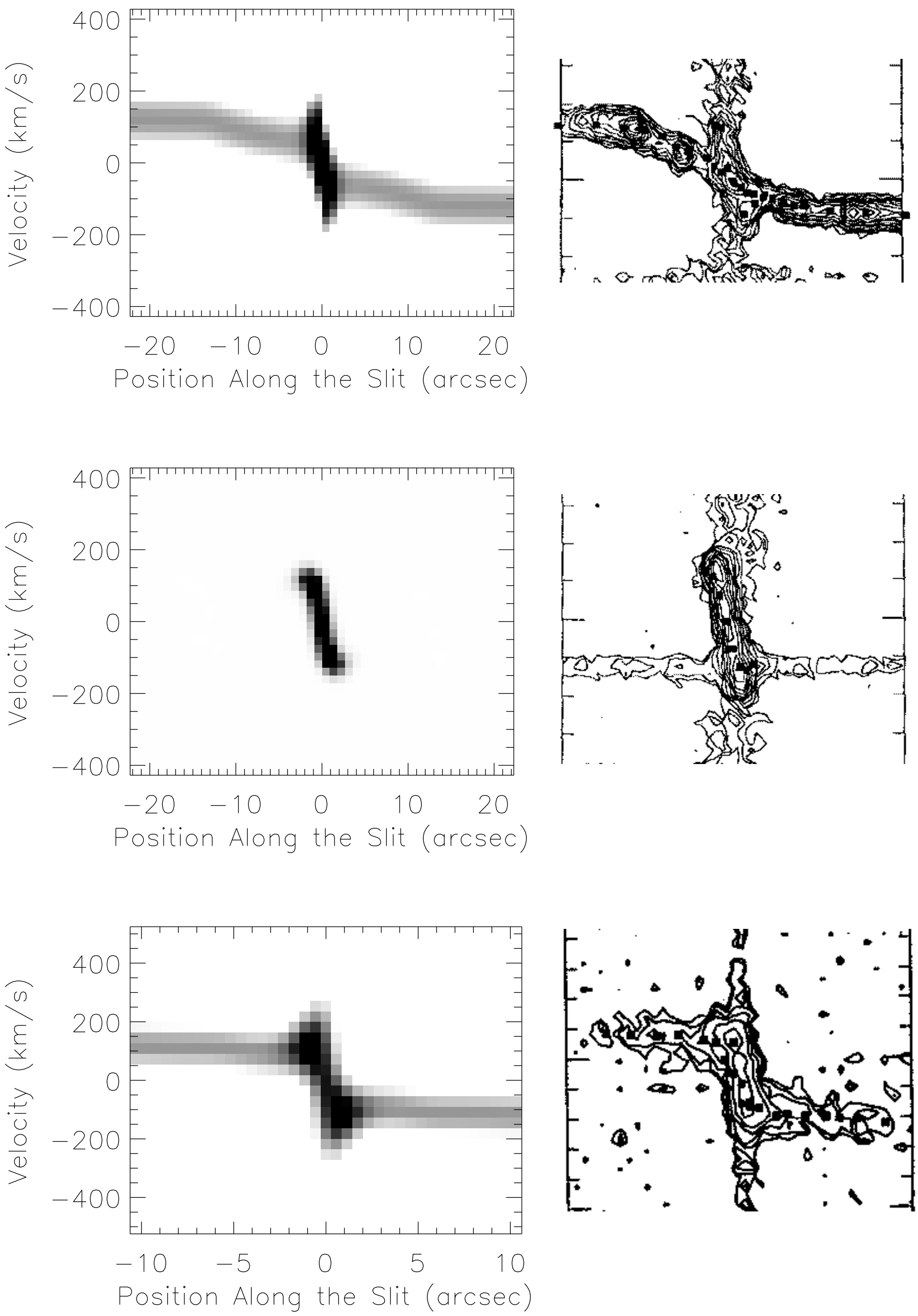

Figure 4.5: Best-fit models (*left column*) of the Hα emission lines observed (their isophotal maps with the same scale are shown in the *right column*) by Rubin et al. (1997) along the major axis of NGC 4343 (*top panels*), NGC 4435 (*middle panels*) and NGC 4459 (*bottom panels*).

4.4 Discussion

In the previous paragraphs we have shown that the peculiar bidimensional shape of the emission lines in a sample of four galaxies is consistent with the effect produced by the combined potential of a central point-like mass and of an extended component. In this way we were able to point out the presence of central mass concentrations of the order of 10^9 $M_\odot$ in a sample of disk galaxies, observed with ground-based telescopes.

With the observations presented in this Chapter we demonstrate the possibility of detecting central mass concentrations in galaxies with ground-based telescopes properly equipped using the CNKDs as probes. The masses which can be detected in this way are larger than 5×10^7 $M_\odot$ at the distance of the Virgo cluster. Up to now the higher resolution offered by HST has not contributed to the detection, using CNKDs, of central masses lower than this limit. In fact the four galaxies so far studied with HST posses central masses of the same order of ours. A simulation similar to the one used in this Chapter predicts that HST, equipped with the Space Telescope Imaging Spectrograph will allow to detect central masses down to the level of 5×10^6 $M_\odot$. Note that although VLBI spectroscopy of H_2O masers delivers much higher angular resolution, this technique is limited by the availability of suitably bright sources. We are inclined to think that the detection of lower mass black holes will constitute one of the most proper use of HST, which also allows to put more stringent constraint on the size of the region containing the central mass.

For the four galaxies of this Chapter with positive detection we can summarize our measurements with a single median value of the ratio of the central mass to the luminosity of the bulge component $M_\bullet / L_{B,\, bulge} \sim 0.16$. This value is one order of magnitude larger than the median value derived by Ho (1998) from a sample of 20 objects but still within the scatter. If we assume for $M_\bullet$ of NGC 5064 the upper limit we derived, also this galaxy falls within the scatter of the relation $M_\bullet - L_{B,\, bulge}$ (Ho 1998).

Bibliography

Bower, G.A., Green, R.F., Danks, A., Gull, T., Heap, S., Hutchings, J., Joseph, C., Kaiser, M.E., Kimble, R., Kraemer, S., Weistrop, D., Woodgate, B., Lindler, D., Hill, R.S., Malumuth, E.M., Baum, S., Sarajedini, V., Heckman, T.M., Wilosn, A.S., & Richstone, D.O. 1998, ApJ, 492, L111

de Vaucouleurs, G., de Vaucouleurs, A., Corwin, H.G., Jr., Buta, R.J., Paturel, G., & Fouqué, R. 1991, Third Reference Catalogue of Bright Galaxies (New York: Springer-Verlag) (RC3)

Ferrarese, L., Ford, H.C., & Jaffe, W. 1996, ApJ, 470, 444

Freedman, W.L., Madore, B.F., Mould, J.R., Ferrarese, L., Hill, R., Kennicutt, R.C., Jr., Saha, A., Stetson, P.B., Graham, J.A., Ford, H., Hoessel, J.G., Hucra, J., Hughes, S.M., & Illingworth, G.D. 1994, Nature, 371, 757

Greenhill, L.J., & Gwinn, C. 1997, Ap&SS, 248, 261

Greenhill, L.J, Moran, J.M., & Herrnstein, J.R. 1997, ApJ, 481, L23

Ho, L.C. 1998, in Observational Evidence for Black Hole in the Universe, ed. S.K. Chakrabati (Dodrecht: Kluver Academic Publishers), in press [astro-ph/9803307]

Kormendy, J., & Richstone, D. 1995, ARA&A, 33, 581

Macchetto, F., Marconi, A., Axon, D.J., Capetti, A., Sparks, W., & Crane, P. 1997, ApJ, 489, 579

Miyoshi, M., Moran, J., Herrnstein, J., Greennhill, L.J., Nakai, N., Diamond, P., & Inoue, M. 1995, Nature 373, 127

Rubin, V.C., Kenney, J.D.P., & Young, J.S. 1997, AJ, 113, 1250

Sandage, A., & Tammann, G.A. 1981, A Revised Shapley-Ames Catalog of Bright Galaxies (Washington: Carnagie Institution)

Simien, F., & de Vaucouleurs, G. 1986, ApJ, 302, 564

Tully, R.B. 1988, Nearby Galaxies Catalog (Cambridge: Cambridge University Press)

van der Marel, R.P., & van den Bosch, F.C. 1998, AJ, submitted [astro-ph/9804194]